Pedestal microdisks in potassium yttrium double tungstate

SIMEN M. MARTINUSSEN,[1,*] **RAIMOND N. FRENTROP,**[1]
MEINDERT DIJKSTRA,[1] **FRANS SEGERINK,**[1] **VICTORIA
TORMO-MÁRQUEZ,**[2] **JOSÉ OLIVARES,**[2] **AND SONIA M.
GARCIA-BLANCO**[1]

[1]*Optical Sciences Group, MESA+ Institute for Nanotechnology, University of Twente, P.O. Box 217,
7500 AE Enschede, The Netherlands*
[2]*Centro de Micro-Análisis de Materiales, Universidad Autónoma de Madrid, E-28049-Madrid, Spain*
*s.m.martinussen@utwente.nl

Abstract: $KY(WO_4)_2$ is an attractive material for integrated photonics due to its high refractive index and excellent non-linear and gain characteristics. High refractive index contrast structures increase light-matter interaction, reducing the threshold for lasing and non-linear effects. Furthermore, high refractive index contrast permits dispersion engineering for non-linear optics. In this work, we present a novel fabrication method to realize pedestal microdisk resonators in crystalline $KY(WO_4)_2$ material. The fabrication process includes swift heavy ion irradiation of the $KY(WO_4)_2$ with 9 MeV carbon ions and sufficient fluence ($>2.7\cdot10^{14}$ ion/cm^2) to create a buried amorphous layer. After annealing at 350° C, microdisks are defined by means of focused ion beam milling. A wet etching step in hydrochloric acid selectively etches the amorphized barrier producing a pedestal structure. The roughness of the bottom surface of the disk is characterized by atomic force microscopy.

1. Introduction

Potassium yttrium double tungstate ($KY(WO_4)_2$) is a member of the potassium double tungstate family of materials. These include, among others, $KY(WO_4)_2$, $KYb(WO_4)_2$, $KGd(WO_4)_2$ and $KLu(WO_4)_2$, which have long been used as bulk laser materials [1–6]. They have several properties that make them very attractive for integrated optics. The refractive index of undoped $KY(WO_4)_2$ ranges between 1.96-2.09 for wavelengths extending from 400 nm to 1550 nm [7]. Such high refractive index enables a high index contrast against common materials such as SiO_2, water and air. Correspondingly, the non-linear refractive index, n_2, is relatively high at 2.4×10^{-19} m^{2}W^{-1} at a wavelength of 819 nm [8], which is comparable to the non-linear refractive index of Si_3N_4 at 1550 nm [9] and lower than that of silicon rich nitride [10]. Furthermore, $KY(WO_4)_2$ has a high Raman gain value with sharp peaks at 765 cm^{-1} and 905 cm^{-1} [11], which has been exploited for the realization of Raman lasers [12].

$KY(WO_4)_2$, when doped with rare-earth ions, exhibits excellent gain characteristics. Rare earth ions doped into the crystal have high transition cross-sections [13]. Since they are substitutionally placed in a large unit cell, a minimum interionic distance between rare-earth ions of >0.4 nm is guaranteed. This reduces quenching compared with amorphous host materials, permitting to heavily dope the material before detrimental quenching effects appear. High dopant concentration has led to the experimental demonstration of ~800 dB/cm gain in an Yb^{3+} doped layer [13] and ~12 dB/cm in an Er^{3+}-doped waveguide amplifier [14]. Several waveguide lasers operating at different wavelength ranges have been demonstrated in this low refractive index contrast waveguide configuration [15,16].

However, a low refractive index contrast structure does not permit achieving anomalous dispersion over a wide range of wavelengths in the near infrared. High refractive index contrast waveguides do permit dispersion engineering, and exhibit high field confinement, which enhances light-matter interaction and therefore reduces the threshold for nonlinear effects. High refractive index contrast also permits the realization of tight bends and ring resonator structures, which further enhances nonlinear effects, reducing the threshold for the generation of frequency combs and cascaded Raman lasers [17–19].

Recently, two techniques have been proposed for creating a thin $KY(WO_4)_2$ layer with high refractive index contrast with respect to the substrate. In the first approach, a $KY(WO_4)_2$ crystal is bonded to a glass carrier, before being lapped and polished to a thickness of <2 µm [20,21]. A refractive index contrast of ~0.5 is achieved using this technique. In the second approach, the crystal is irradiated with carbon ions at an energy of 9 MeV [22]. Due to electronic interactions of the carbon ions with the crystalline material, a layer extending ~1.5-3 µm below the surface is fully amorphized for fluences above $2.7 \cdot 10^{14}$ ion/cm^2. The refractive index of the amorphous layer is ~0.3 lower than the refractive index of the crystalline surface layer core.

The amorphized layer induced by ion irradiation has been reported to exhibit a preferential etching in common wet etching solutions with respect to the undamaged material. Such amorphization-enhanced wet etching has been observed in other systems after both ion irradiation and pulsed laser modification. It has been reported before in several crystalline materials, including $LiNbO_3$ [23], sapphire [24,25] and silicon [26], as well as amorphous materials such as fused silica [27] and Foturan glass [28]. Irradiation followed by selective etching has been used to create structures such as under-etched sheets [24], ridge waveguides [29] and microfluidic channels [27].

In this work, we exploit the selective etching of the irradiation-induced amorphous layer with respect to the undamaged crystalline structure of undoped $KY(WO_4)_2$ to further increase the contrast of the $KY(WO_4)_2$ waveguides by producing a pedestal geometry, in which the mode lies inside a thin $KY(WO_4)_2$ layer surrounded by air. A refractive index contrast of Δn~1 between disk and air is achieved using this method.

2. Fabrication process of pedestal microdisks in $KY(WO_4)_2$

The fabrication process flow for the proposed pedestal microdisks can be seen in Fig. 1. A $KY(WO_4)_2$ slab of dimensions $10 \times 10 \times 1$ mm^3 was purchased from Altechna. One of the 10×10 mm^2 facets of the sample was polished by the manufacturer to an RMS roughness of 1.5 nm. The sample was irradiated with carbon ions accelerated to an energy of 9 MeV in a tandem accelerator, at a total fluence of $3 \cdot 10^{14}$ cm^{-2}.

During irradiation, the samples were attached to the sample holder with copper tape to avoid charging of the non-conductive $KY(WO_4)_2$ substrate. Irradiation was performed at an angle of 5° to avoid channeling. An ion beam area of 3×3 cm^2 was utilized to ensure uniform irradiation of the 1 cm^2 sample. The ion current was kept below 1 µA to prevent heating of the sample. Because the applied fluence is above the amorphization threshold, an amorphized barrier region appears in the substrate at around 1.5-3 µm below the surface, centered around the peak of the electronic stopping power. Another damage region is generated by the nuclear stopping power. The nuclear barrier is much thinner and occurs around 5 µm into the substrate [22]. This work is only concerned with the amorphized electronic barrier. The sample was then annealed at 350°C for 3 hours in order to repair point defects, reduce propagation losses and sharpen the refractive index boundary by repairing partially amorphized $KY(WO_4)_2$ [22]. In future devices, this annealing will be performed after milling to repair any potential damage caused by the gallium ions [30].

A FEI Nova 600 NanoLab DualBeam focused ion beam (FIB) system with Ga$^+$ ions at an acceleration voltage of 30 kV and a current of 21 nA was utilized to pattern disks, with a milling
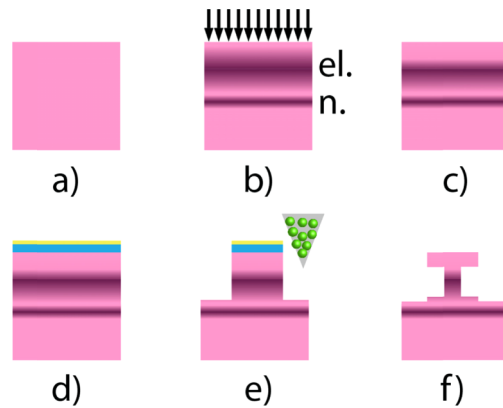
Fig. 1. Complete process flow. (a) Virgin KY(WO$_4$)$_2$ substrate. (b) Ion irradiation creates a refractive index gradient. The electronic barrier is marked by "el." and the nuclear barrier is marked by "n.". (c) Thermal annealing removes point defects and repairs the KY(WO$_4$)$_2$ that is only partially amorphized, which makes the refractive index profile more step-like. (d) Overgrowth with protective PECVD SiO$_2$ (in blue) and AuPd SEM coating (in yellow). (e) FIB milling with 30 keV Ga$^+$ ions and a current of 21 nA. (f) Wet etching with HCl and TMAH followed by SiO$_2$ removal with HF. The top of the sample contains an unetched disk. Beneath it is an underetched region.

depth of 5 μm or more (Fig. 2). Sufficient milling depth is necessary in order to expose the amorphized barrier and give access to the etching solution. The milling direction was towards the disk, in order to avoid re-deposition on the sidewalls of the milled structure. A 300 nm PECVD SiO$_2$ layer was grown on the sample to protect the top surface from the etchant, and a 5 nm AuPd layer was sputtered before milling to avoid charging.
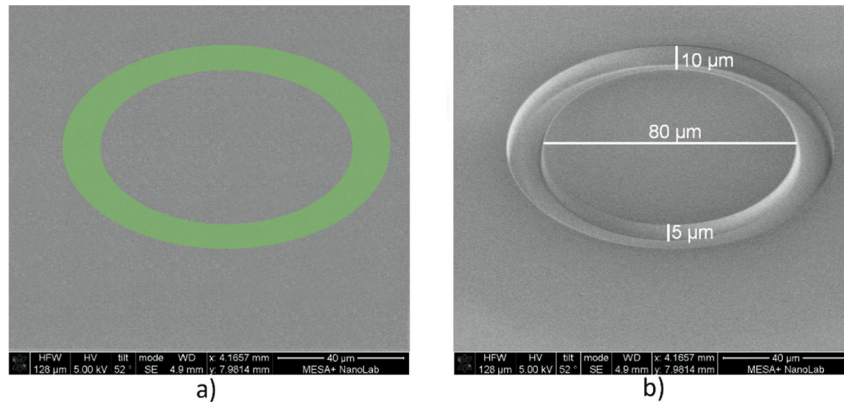

Fig. 2. a) Overlay of SEM image and FIB pattern. The green ring represents the material to be milled. b) Resulting FIB milled microdisk in KY(WO$_4$)$_2$.

Preferential wet etching was then performed using a 20% HCl solution at room temperature. Although crystalline KY(WO$_4$)$_2$ is a chemically inert material, there are references to ion exchange reactions at elevated temperatures [31]:

$$KY(WO_4)_2 + 4\,HCl \xrightarrow{100°C} KCl + YCl_3 + 2\,WO_3 + 2\,H_2O \tag{1}$$
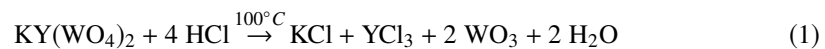
While this reaction only occurs near the boiling point of HCl in crystalline $KY(WO_4)_2$, we demonstrate in this work that 20% HCl is effective at room temperature to etch the amorphized region. Looking at (1), a potential issue is the reaction product WO_3, which is insoluble in water.

The resulting structure after 6 hours of etching was imaged by means of FIB cross-sectioning and SEM (Fig. 3). A significant amount of underetching was observed. However, residues after the etching step can be seen (Fig. 3(a)). The residues produced clogging of the opening and prevented further access to the HCl etching solution. It is hyphothized that the residues are WO_3 produced during the etching of amorphous $KY(WO_4)_2$ in HCl (Eq. 1).

a)   b)
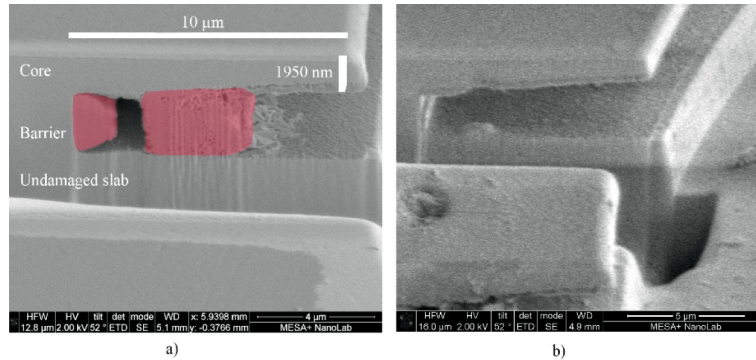
Fig. 3. (a) FIB cross-section of a $KY(WO_4)_2$ disk etched in 20% HCl for 6 hours. The wet etching process is effective at reaching deep into the material. The etching is faster at the interfaces of the barrier, as indicated on the left edge of the cavity. A large amount of unetched material remains and has been artificially colored. (b) The same sample after 1 hour of etching in 25% TMAH. The residues have been completely removed, including the coating on the bottom side of the core as well as the wedge shape on the left.

The residues were investigated using microRaman spectroscopy. The measured spectrum (Fig. 4) showed peaks at 261 cm^{-1}, 708 cm^{-1}, and 804 cm^{-1}, which are within the range of peaks associated to WO_3 nanocrystals between 4 and 35 nm [32]. Since WO_3 is soluble in alkaline
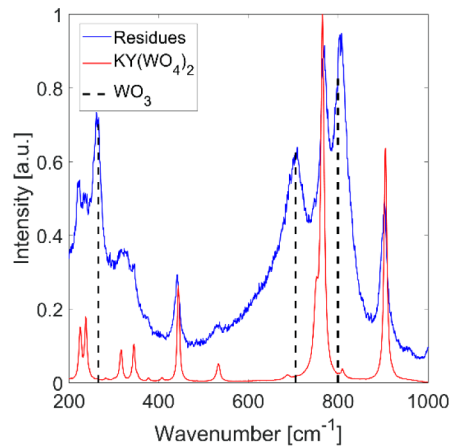
Fig. 4. Raman spectrum of residues compared with crystalline $KY(WO_4)_2$ from the same sample with laser polarization E||c, differentiated by the depth of the focus. The Raman peaks associated with 16 nm WO_3 nanocrystals are indicated with dashed lines at 265 cm^{-1}, 705 cm^{-1}, and 799 cm^{-1} [32].

solutions [33], an etching step in 25% TMAH at room temperature was implemented. The sample was again imaged after etching for 1 hour in TMAH in order to verify the effectiveness in the removal of the WO_3 residues. Fig. 3(b) shows the cross-section of the disk after the TMAH etching step. TMAH successfully removed the residues, both the clog as well as the thin WO_3 layer on the bottom side of the $KY(WO_4)_2$ suspended core.

An optimized etching process was implemented. The HCl concentration was increased to 32% and the HCl and TMAH steps were performed twice. The sample was etched in 32% HCl for 2 hours, followed by a cleaning step of 1 hour in TMAH. This process was repeated twice (i.e., 2 hours in HCl, 1 hour in TMAH, 2 hours in HCl and 1 hour in TMAH) to achieve a total underetch of 29 μm. After wet etching, the sample was dried using the cyclohexane freeze drying technique [34]. In this method the etchant is gradually and sequentially diluted and replaced with water, acetone and finally cyclohexane, which is sublimated at -5° C. Freeze drying avoids cracking of free standing features due to the capillary forces induced by the drying water. The pedestal disks were imaged with the SEM in the DualBeam FIB using 2 kV acceleration voltage (Fig. 5).
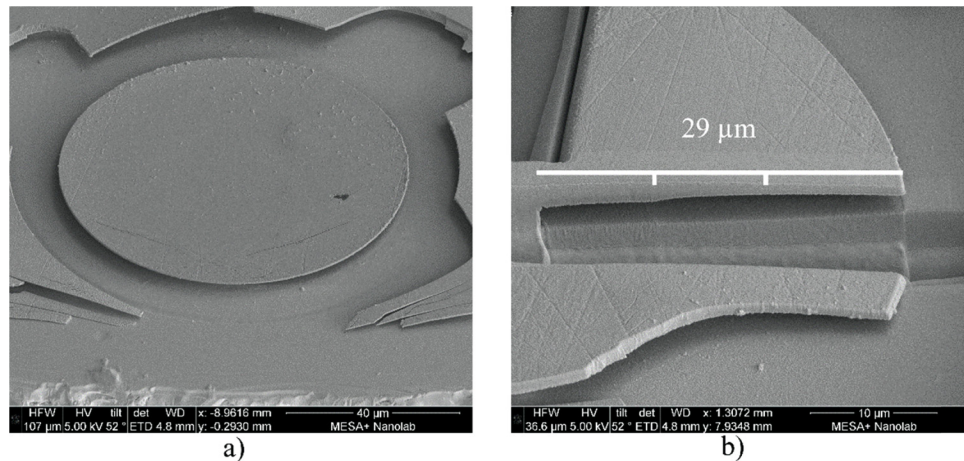
Fig. 5. (a) SEM image of a 80 μm diameter pedestal disk in $KY(WO_4)_2$ after two rounds of 32% HCl for two hours, each of them followed by a 25% TMAH etching step for one hour. (b) Cross section of a $KY(WO_4)_2$ sample that has been etched for two rounds of two hours in 32% HCl and 1 hour in 25% TMAH. The horizontal depth of the underetch is 29 μm, the vertical depth is 3 μm and the disk is 1 μm thick throughout the outer 10 μm of the disk. The approximate boundaries between the initial etch, the transition region and the final etch are indicated by notches.

## 3.   Characterization of the pedestal microdisks

A cross-section of the structure after FIB milling and two cycles of 2 hours etching in 32% HCl at room temperature followed by 1 hour of 25% TMAH is shown in Fig. 5 (b). An underetch of 29 μm was measured, which corresponds to an etch rate of ∼120 nm/min. However, the cross section is divided into two segments of different thicknesses. The outer segment exhibits an uniform thickness of ∼1 μm. The layer gradually tapers, starting at 10 μm from the edge, indicating incomplete removal of the amorphized region. The outer thickness corresponds to the undamaged (crystalline) region predicted by SRIM simulations [22]. The high selectivity between the undamaged core area and amorphized barrier leads to a self-stopped wet etch. The subsequent TMAH cleaning further removes the WO_3 residues from the bottom side of the core. An etch rate of 158 nm/min can be calculated for this region.

Between 19 μm and 29 μm the thickness is uniform at 2 μm. This second region is attributed to the second HCl etching step, which proceeded at a lower etching rate due to restricted diffusion, even though the etchant solutions were identical. The higher thickness of this segment suggests that the etching step was not self-terminated, and amorphous material is still present. However, calculations show that any under-etch above 4 μm is more than sufficient to have a highly confined mode in the outer rim of the microdisk at an operation wavelength of 1550 nm [35].

In order to investigate the roughness of the bottom of the disks, a destructive tape peeling technique was used in combination with AFM. RevAlpha 3195 tape was pressed onto the sample and peeled off in order to release the disks and expose the bottom surface, shown in Fig. 6. A Bruker Dimension ICON AFM was used to inspect the sample using a triangular ScanAsyst-Air probe with a tip radius of 4 nm in PeakForce Tapping mode. The resulting AFM image is shown in Fig. 7. The root mean square (RMS) roughness is 23.4 nm, measured in three locations of the sample, each 1.5×1.5 μm^2, and the bottom to peak height difference is 165.6 nm. Such high roughness will induce high propagation losses. Therefore, improved fabrication methods that will permit reducing such roughness are currently being investigated.
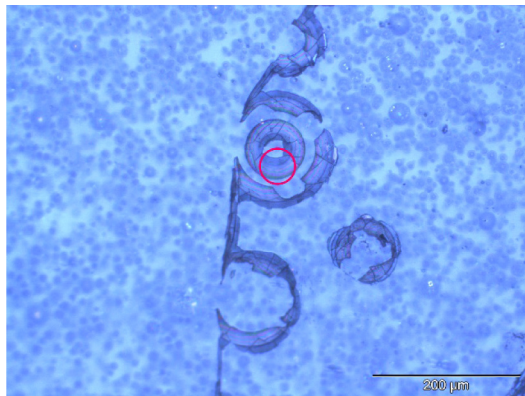
Fig. 6. Remaining KY(WO$_4$)$_2$ structures after transfer to adhesive tape. The center of the disk has not been transferred because it is firmly attached to the pedestal. The underetched area surrounding the disk, also visible in Fig. 5 a), has also been transferred. The area of main interest is indicated by the red circle, selected for its lack of cracks.
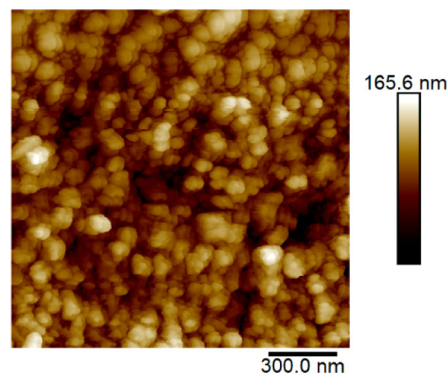
Fig. 7. AFM image of a 1.5 μm by 1.5 μm section of the underside of the disk in Fig. 2. The image was made close to the edge of the disk.

4.   Summary

In this work, we report the first realization of pedestal structures in crystalline $KY(WO_4)_2$. The process is based on the selectivity of an HCl wet etching step between the crystalline and amorphized $KY(WO_4)_2$ after swift carbon ion irradiation with an energy of 9 MeV and a fluence ($3 \cdot 10^{14}$ ion/cm^2) above the amorphization threshold. WO_3 residues were produced during the etching step that limited the depth of the under-etch. A cleaning step in TMAH cleaned the structure from WO_3 residues and permitted to extend the etching further. The proposed technology paves the road towards the fabrication of high-refractive index constrast pedestal structures for highly efficient non-linear devices once the roughness on the inner surface of the pedestal is drastically reduced.

References

1. A. A. Kovalyov, V. V. Preobrazhenskii, M. A. Putyato, O. P. Pchelyakov, N. N. Rubtsova, B. R. Semyagin, V. E. Kisel', S. V. Kuril'chik, and N. V. Kuleshov, "115 fs pulses from Yb^{3+}:KY(WO$_4$)$_2$ laser with low loss nanostructured saturable absorber," Laser Phys. Lett. **8**(6), 431–435 (2011).
2. A. A. Lagatsky, F. Fusari, S. Calvez, J. A. Gupta, V. E. Kisel, N. V. Kuleshov, C. T. A. Brown, M. D. Dawson, and W. Sibbett, "Passive mode locking of a Tm,Ho:KY(WO$_4$)$_2$ laser around 2 μm," Opt. Lett. **34**(17), 2587–2589 (2009).
3. F. Brunner, G. J. Spühler, J. A. Au, L. Krainer, F. Morier-Genoud, R. Paschotta, N. Lichtenstein, S. Weiss, C. Harder, A. A. Lagatsky, A. Abdolvand, N. V. Kuleshov, and U. Keller, "Diode-pumped femtosecond Yb:KGd(WO$_4$)$_2$ laser with 1.1-W average power," Opt. Lett. **25**(15), 1119–1121 (2000).
4. U. Griebner, S. Rivier, V. Petrov, M. Zorn, G. Erbert, M. Weyers, X. Mateos, M. Aguiló, J. Massons, and F. Díaz, "Passively mode-locked Yb:KLu(WO$_4$)$_2$ oscillators," Opt. Express **13**(9), 3465–3470 (2005).
5. V. Petrov, M. Cinta Pujol, X. Mateos, Ò. Silvestre, S. Rivier, M. Aguiló, R. M. Solé, J. Liu, U. Griebner, and F. Díaz, "Growth and properties of KLu(WO$_4$)$_2$, and novel ytterbium and thulium lasers based on this monoclinic crystalline host," Laser Photonics Rev. **1**(2), 179–212 (2007).
6. A. A. Kaminskii, P. V. Klevtsov, L. Li, and A. A. Pavlyuk, "Stimulated emission from KY(WO$_4$)$_2$: Nd^{3+} crystal laser," Phys. Status Solidi A **5**(2), K79–K81 (1971).
7. S. Aravazhi, D. Geskus, K. van Dalfsen, S. A. Vázquez-Córdova, C. Grivas, U. Griebner, S. M. Garcia-Blanco, and M. Pollnau, "Engineering lattice matching, doping level, and optical properties of KY(WO$_4$)$_2$:Gd, Lu, Yb layers for a cladding-side-pumped channel waveguide laser," Appl. Phys. B: Lasers Opt. **111**(3), 433–446 (2013).
8. N. Thilmann, G. Strömqvist, M. C. Pujol, V. Pasiskevicius, V. Petrov, and F. Díaz, "Nonlinear refractive indices in Yb^{3+}-doped and undoped monoclinic double tungstates KRE(WO$_4$)$_2$ where RE = Gd, Y, Yb, Lu," Appl. Phys. B: Lasers Opt. **96**(2-3), 385–392 (2009).
9. K. Ikeda, R. E. Saperstein, N. Alic, and Y. Fainman, "Thermal and Kerr nonlinear properties of plasma-deposited silicon nitride/silicon dioxide waveguides," Opt. Express **16**(17), 12987–12994 (2008).
10. C. J. Krückel, A. Fülöp, T. Klintberg, J. Bengtsson, P. A. Andrekson, and V. Torres-Company, "Linear and nonlinear characterization of low-stress high-confinement silicon-rich nitride waveguides," Opt. Express **23**(20), 25827–25837 (2015).
11. J. A. Piper and H. M. Pask, "Crystalline Raman Lasers," IEEE J. Sel. Top. Quantum Electron. **13**(3), 692–704 (2007).
12. Z. Cong, Z. Liu, Z. Qin, X. Zhang, H. Zhang, J. Li, H. Yu, and W. Wang, "LD-pumped actively Q-switched Nd:KLu(WO$_4$)$_2$ self-Raman laser at 1185 nm," Opt. Laser Technol. **73**, 50–53 (2015).
13. Y.-S. Yong, S. Aravazhi, S. A. Vázquez-Córdova, J. J. Carvajal, F. Díaz, J. L. Herek, S. M. Garcia-Blanco, and M. Pollnau, "Direct confocal lifetime measurements on rare-earth-doped media exhibiting radiation trapping," Opt. Mater. Express **7**(2), 527–532 (2017).
14. S. A. Vázquez-Córdova, S. Aravazhi, C. Grivas, Y.-S. Yong, S. M. Garcia-Blanco, J. L. Herek, and M. Pollnau, "High optical gain in erbium-doped potassium double tungstate channel waveguide amplifiers," Opt. Express **26**(5), 6260–6266 (2018).

15. K. van Dalfsen, S. Aravazhi, C. Grivas, S. M. Garcia-Blanco, and M. Pollnau, "Thulium channel waveguide laser with 1.6 W of output power and ~80% slope efficiency," Opt. Lett. **39**(15), 4380–4383 (2014).

16. D. Geskus, S. Aravazhi, C. Grivas, K. Wörhoff, and M. Pollnau, "Microstructured $KY(WO_4)_2$:Gd^{3+}, Lu^{3+}, Yb^{3+} channel waveguide laser," Opt. Express **18**(9), 8853 (2010).

17. G. Lin, A. Coillet, and Y. K. Chembo, "Nonlinear photonics with high-Q whispering-gallery-mode resonators," Adv. Opt. Photonics **9**(4), 828–890 (2017).

18. S. M. Spillane, T. J. Kippenberg, and K. J. Vahala, "Ultralow-threshold Raman laser using a spherical dielectric microcavity," Nature **415**(6872), 621–623 (2002).

19. B. Min, T. J. Kippenberg, and K. J. Vahala, "Compact, fiber-compatible, cascaded Raman laser," Opt. Lett. **28**(17), 1507–1509 (2003).

20. C. I. van Emmerik, S. M. Martinussen, J. Mu, M. Dijkstra, R. Kooijman, and S. M. Garcia-Blanco, "A novel polishing stop for accurate integration of potassium yttrium double tungstate on a silicon dioxide platform," *Proc SPIE* 10535, 105350U (2018).

21. M. A. Sefunc, F. B. Segerink, and S. M. Garcia-Blanco, "High index contrast passive potassium double tungstate waveguides," Opt. Mater. Express **8**(3), 629–638 (2018).

22. R. N. Frentrop, V. Tormo-Márquez, J. Olivares, and S. M. García-Blanco, "High-contrast slab waveguide fabrication in $KY(WO^4)^2$ by swift heavy ion irradiation," *Proc SPIE 10535*, 105350O (2018).

23. F. Schrempel, T. Gischkat, H. Hartung, E.-B. Kley, and W. Wesch, "Ion beam enhanced etching of $LiNbO_3$," Nucl. Instrum. Methods Phys. Res., Sect. B **250**(1-2), 164–168 (2006).

24. A. Crunteanu, G. Jänchen, P. Hoffmann, M. Pollnau, C. Buchal, A. Petraru, R. W. Eason, and D. P. Shepherd, "Three-dimensional structuring of sapphire by sequential He^+ ion-beam implantation and wet chemical etching," Appl. Phys. A **76**(7), 1109–1112 (2003).

25. L. Capuano, R. Pohl, R. M. Tiggelaar, J. W. Berenschot, J. G. E. Gardeniers, and G. R. B. E. Römer, "Morphology of single picosecond pulse subsurface laser-induced modifications of sapphire and subsequent selective etching," Opt. Express **26**(22), 29283–29295 (2018).

26. S. Lee, K. Jo, H. Keum, S. Chae, Y. Kim, J. Choi, H. H. Lee, and H. J. Kim, "Nanowall formation by maskless wet-etching on a femtosecond laser irradiated silicon surface," Appl. Surf. Sci. **437**, 190–194 (2018).

27. R. Osellame, H. J. W. M. Hoekstra, G. Cerullo, and M. Pollnau, "Femtosecond laser microstructuring: an enabling tool for optofluidic lab-on-chips," Laser Photonics Rev. **5**(3), 442–463 (2011).

28. K. Sugioka, Y. Hanada, and K. Midorikawa, "Three-dimensional femtosecond laser micromachining of photosensitive glass for biomicrochips," Laser Photonics Rev. **4**(3), 386–400 (2010).

29. P. D. Nicola, S. Sugliani, G. B. Montanari, A. Menin, P. Vergani, A. Meroni, M. Astolfi, M. Borsetto, G. Consonni, R. Longone, A. Nubile, M. Chiarini, M. Bianconi, and G. G. Bentini, "Fabrication of Smooth Ridge Optical Waveguides in $LiNbO_3$ by Ion Implantation-Assisted Wet Etching," J. Lightwave Technol. **31**(9), 1482–1487 (2013).

30. L. a. M. Barea, F. Vallini, A. R. Vaz, J. R. Mialichi, and N. C. Frateschi, "Low-roughness active microdisk resonators fabricated by focused ion beam," J. Vac. Sci. Technol., B: Microelectron. Nanometer Struct.–Process., Meas., Phenom. **27**(6), 2979–2981 (2009).

31. Y. Romanyuk, "Liquid-phase epitaxy of doped $KY(WO_4)_2$ layers for waveguide lasers," *Thesis, École Polytechnique Fédérale de Lausanne* (2005).

32. M. Boulova and G. Lucazeau, "Crystallite Nanosize Effect on the Structural Transitions of WO_3 Studied by Raman Spectroscopy," J. Solid State Chem. **167**(2), 425–434 (2002).

33. D. R. Lide, *CRC Handbook of Chemistry and Physics: A Ready-Reference Book of Chemical and Physical Data* (CRC-Press, 1995).

34. R. Legtenberg and H. A. C. Tilmans, "Electrostatically driven vacuum-encapsulated polysilicon resonators Part I. Design and fabrication," Sens. Actuators, A **45**(1), 57–66 (1994).

35. S. M. Martinussen, R. N. Frentrop, M. Dijkstra, F. Segerink, V. Tormo-Márquez, J. Olivares, and S. M. Garcia-Blanco, "Pedestal disk resonator in potassium yttrium double tungstate," *Proc SPIE 10535*, 105350Q (2018).